Icarus **151**, 275–285 (2001)
doi:10.1006/icar.2001.6603, available online at http://www.idealibrary.com on IDEAL®

EPIC Simulations of Bright Companions to Neptune's Great Dark Spots

P. W. Stratman

Comparative Planetology Laboratory, University of Louisville, Louisville, Kentucky 40292

A. P. Showman

National Research Council/NASA Ames Research Center, Moffett Field, California 94035

T. E. Dowling

Comparative Planetology Laboratory, University of Louisville, Louisville, Kentucky 40292
E-mail: dowling@louisville.edu

and

L. A. Sromovsky

Space Science and Engineering Center, University of Wisconsin, Madison, Wisconsin 53706

Received March 27, 2000; revised February 2, 2001

We present a three-dimensional model of the bright companion clouds associated with Neptune's Great Dark Spots (GDSs). Our results support the hypothesis that the bright companions of the southern-hemisphere GDS discovered in 1989 and of the northern-hemisphere GDS discovered in 1994 are methane clouds that form at or just below the tropopause and that they are caused by lifting in a manner analogous to the formation of orographic clouds. We vary the vertical position of the GDS and find that the companion cloud is a robust feature except when the anticyclone itself does not survive. When a GDS is started with its top in the stratosphere it drifts much too rapidly toward the equator and quickly disperses. On the other hand, if its top is well below the tropopause there is a tendency for the companion clouds to be too large. Hence the top of a GDS is probably at the tropopause. Along an open streamline that threads a bright companion, the typical pressure and temperature drops are about 3 mb and 1 K, respectively, corresponding to a lift of about half a kilometer or 4% of the pressure scale height, and the relative horizontal wind speed is about 45 m s^{-1} eastward through the cloud.

Key Words: **atmospheric dynamics; atmospheric structure; meteorology; Neptune; atmosphere.**

1. INTRODUCTION

We model a persistent cloud formation found on Neptune—the large, bright-white companion cloud associated with each of the two Great Dark Spots observed to date, GDS-89 and GDS-94—and explore whether this feature's existence places useful constraints on Neptune's atmosphere. Many details have been established about the chemical makeup of clouds, aerosols, and hazes on Neptune (Baines *et al.* 1995a), but these cloud models have been generally restricted to one dimension (height) for chemical modeling (e.g., Stoker and Toon 1989, Romani *et al.* 1993, Baines and Hammel 1994), or no dimensions (no vertical structure) for the estimation of cloud microphysical timescales (Carlson *et al.* 1988). Additional information on dynamical and chemical processes may be obtained by simulating the clouds of Neptune and the other gas giants in a global, three-dimensional model.

As a general rule, clouds are easy to observe but hard to represent in large-scale models (Tiedtke 1993). Different cloud types are associated with different amounts of precipitation, latent heating, and optical depth, and it is common for more than one cloud type to be present in the volume enclosed by a model grid cell. The computational burden can be large; for example, terrestrial mesoscale models employ five coupled continuity equations just to handle the conversion of water substance between water vapor, cloud liquid, cloud ice, rain, and snow (e.g., Thompson *et al.* 1997), and additional prognostic equations are needed if cloud particle sizes are to be distinguished. For these reasons, in practice most cloud processes must be parameterized rather than explicitly resolved in general circulation models (GCMs), a consistent treatment of which has yet to emerge (Xu and Randall 1996).

Nevertheless, there is merit in the effort to adapt terrestrial cloud schemes to planetary GCMs. Here, we initiate this effort for gas-giant GCMs with a simple problem that uses clouds as

0019-1035/01 $35.00

probes of the dynamics, but one for which most of the complicating effects associated with clouds are secondary. Neptune's bright companions fall into this class for the following reasons. First, their appearance suggests that they may be orographic in nature, meaning that they are formed by moist air that is forced to rise over the top of the GDS (Smith *et al.* 1989), and latent heating plays only a secondary role for such clouds on Earth (Houze 1994). Second, the bright companion cloud is large enough to be explicitly resolved by our model. Third, Neptune's heat flux is 0.003 times that of Earth, which implies a radiative relaxation timescale of 80 years at the 1-bar level such that cloud-induced radiative heating and cooling are negligible on the weeks-to-months timescales we consider here.

A collection of GDS companion-cloud observations is displayed in Fig. 1. The top sequence of eight images spans an 8-day oscillation cycle of the Voyager-encounter Great Dark Spot, hereafter called the GDS-89. The bright companion is the long white cloud rimming the poleward edge of the GDS-89 (the bottom edge). It is nearly always present. Also usually present are the long clouds to the immediate east and west of the anticyclone. A persistant cloud as large as the bright companion was not seen rimming the equatorward edge, but occasionally long, thin clouds form the appearance of a broken ellipse that includes the equatorward side (as in the panels labeled "4.55" and "5.28" in Fig. 1). An interesting question is what causes the asymmetry of the cloud patterns on the poleward and equatorward halves of the GDS.

During the Voyager encounter the GDS-89 was heading toward Neptune's equator at a rate of 1.3°/month, and it would have arrived in November 1990 had that rate continued (Sromovsky *et al.* 1993). Modeling by LeBeau and Dowling (1998) suggests that it probably dispersed shortly after crossing inside of 15° latitude. The demise of the vortex was not observed, but there has been no detection of a southern-hemisphere bright companion or GDS in any Hubble space telescope (HST) observing opportunities since that time. Instead, a new dark spot discovered in 1994 in HST images (Hammel *et al.* 1995), hereafter called GDS-94, has emerged in the northern hemisphere. Observations of the GDS-94 are shown in the bottom sequence of images in Fig. 1. Starting at the left, the alternating filters reveal the GDS-94 and its bright companion in 1994, and again in 1996, the second pair presumably, but not certainly, the same object. The fifth panel is a Voyager image of the GDS-89 flipped across the equator for comparison. Sromovsky *et al.* (2001) discuss the intriguing white clouds that often appear along the line between each GDS and the equator, which can be seen in the second and fifth bottom panels.

Smith *et al.* (1989) first tendered the hypothesis we are testing: "The bright companion may be similar to orographic clouds observed on Earth, that is, clouds created by air being forced upward by the presence of a mountain. Specifically, the smallest features appeared to move relative to the structure as a whole. The role of topography, necessary for the formation of terrestrial orographic clouds, may be played by temperature and pressure anomalies associated with the GDS." We test this hypothesis by numerically solving the three-dimensional primitive equations using the Explicit Planetary Isentropic Coordinate (EPIC) model of Dowling *et al.* (1998), which has been recently used to study Neptune's Great Dark Spots (LeBeau and Dowling 1998) and Jupiter's 5-μm hot spots (Showman and Dowling 2000). As a guide to what follows, we find the answers to the following three questions to be "yes," "somewhat," and "yes": (i) Will an orographic-style methane cloud form over a model GDS? (ii) Is the cloud's vertical and horizontal position and size diagnostic of the vertical position of the GDS? (iii) Does the cloud's existence place constraints on the methane relative humidity in Neptune's upper troposphere?

2. DESIGN OF EXPERIMENTS

The gist of the experiments is that we add methane vapor to a Neptune EPIC model that has a GDS similar to that studied by LeBeau and Dowling (1998), and then track the vapor's relative humidity (RH) as it interacts with the vortex. Potential temperature, θ, is chosen to be the model's vertical coordinate, rather than geometric height, z, or pressure, p, because it has been demonstrated to be the most accurate coordinate for modeling the long-range transport of water vapor in Earth models (Johnson *et al.* 1993).

The modifications to LeBeau and Dowling's model are as follows. They used idealized temperature profiles, $T(p)$, their Fig. 3a, to obtain idealized stratifications characterized by constant squared buoyancy frequency, N^2, whereas we use the Voyager radio-occultation $T(p)$ with helium at 19% mole fraction, shown as the dotted curve in Fig. 2 (digitized from Fig. 1 of Conrath *et al.* 1991). To increase grid resolution, we reduce the physical domain size in all three directions while maintaining about the same number of grid points (Table I), and the layers are spaced proportionally to $\log\theta$ instead of $\log p$, which yields three layers (vertical index $k = 6, 7,$ and 8 in Fig. 2) that intercept the methane-cloud altitudes compared to one with $\log p$ spacing. The black diamonds in Fig. 2 indicate the temperature–pressure values in the model's unperturbed θ layers (i.e., those away from the vortex), and the solid curve connecting them shows how the vertical resolution around the tropopause is increased at the expense of that deeper down. Both studies assume the basic-state (unperturbed) zonal wind u is constant with height and is in gradient balance with the basic-state pressure field; but while LeBeau and Dowling studied a series of idealized $u(\lambda)$ profiles that produce linear variations of absolute vorticity with respect to latitude, λ, we use the spherical harmonic fit to the cloud-drift data listed in LeBeau and Dowling's Table V to initialize $u(\lambda)$.

2.1. Initial Methane Distribution

In the model, we take Neptune's dry air to be 81% H_2 and 19% He by mole and the para-hydrogen fraction to be frozen at the deep (high-temperature) value of 0.25. The model's prognostic

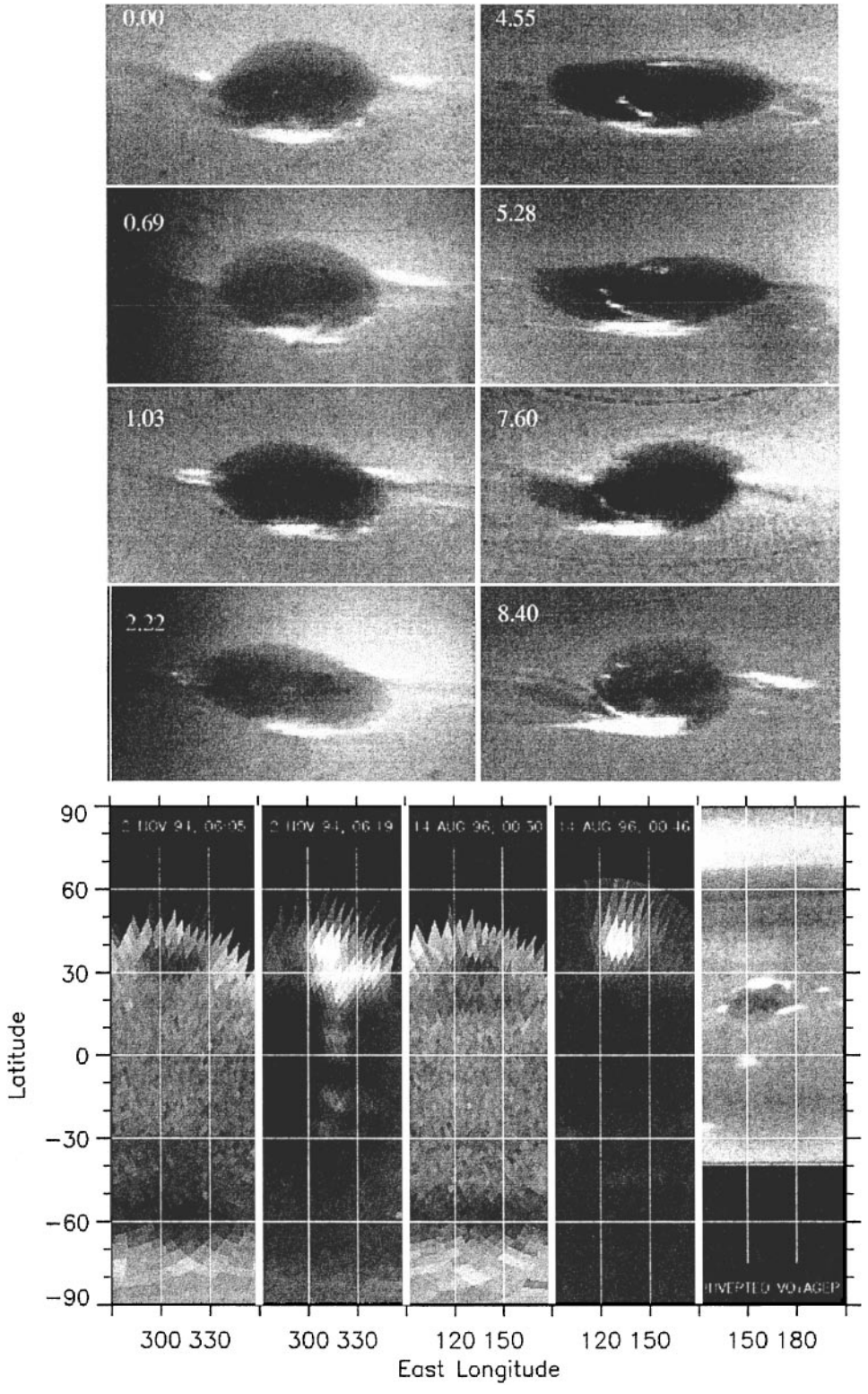

FIG. 1. Observations of bright companions to Neptune's Great Dark Spots. The upper eight panels, adapted from Sromovsky *et al.* (1993), are Voyager observations covering one 8-day oscillation period of the GDS-89. Each is a cylindrical projection spanning 75° in longitude and 30° in latitude; the time is days after day 227 of 1989 (1 day = 24 hours). The first six panels are made with the narrow-angle camera using a clear filter and the last two with the wide-angle camera and blue and green filters, respectively. The lower five panels, adapted from Sromovsky *et al.* (2001), are HST observations from 1994 and 1996, except the rightmost one, which is a Voyager green-filter image inverted across the equator for comparison. The leftmost two are from 2 Nov 1994, while the third and fourth are from 14 Aug 1996. The first and third images, made with the HST F467M filter, are corrected for limb darkening to enhance the contrast of the GDS-94 centered near 35° N. The second and fourth images, made with 890-nm and 621-nm filters, respectively, provide high-contrast views of bright companion clouds.

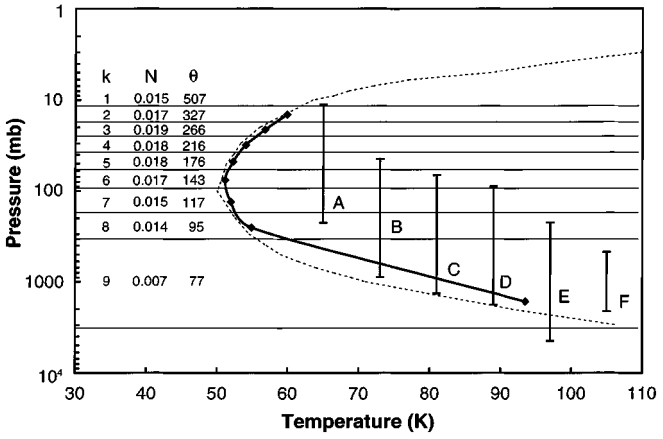

FIG. 2. Model vertical structure and resolution. The dotted curve is the Voyager radio occultation $T(p)$ profile assuming 19% helium mole fraction. It is used to initialize the temperature and pressure values in each of the model's unperturbed potential-temperature layers as indicated by the black diamonds connected by a solid curve. On the left, three data columns list the corresponding layer values of the vertical index, k, the buoyancy frequency, N [s^{-1}], and the potential temperature, θ [K], which is the vertical coordinate. Layers are spaced proportionally to $\log\theta$ to increase vertical resolution in the tropopause region; the horizontal lines show the initial layer-interface pressures. On the right, various cases for the initial vertical positions for the model GDS are indicated by the vertical bars labeled A–F with their tops and bottoms at plus or minus the semi-minor axis, c.

variable for methane is specific humidity (the mass of methane vapor divided by the total mass). The two continuity equations for total mass and methane specific humidity are integrated using the positive-definite scheme of Hsu and Arakawa (1990).

To set the initial distribution of methane vapor, we start by choosing a methane mole fraction for the deepest layer. Overlying layers are assigned this mole fraction as long as their relative humidity is less than 100%; when saturation is reached the initial mole fraction is set to follow the saturation curve. Because the volume enclosed by a grid cell may contain substantial cloudiness and yet have an average relative humidity that is less than 100%, in a subset of experiments we varied the above scheme by following the saturation curve times a fraction $\alpha < 100\%$. At levels near and above the temperature minimum (tropopause), the predicted saturation mole fraction (times α) may exceed that in the layer below; if so, we use the mole fraction of the layer below. This mimics the effect of a tropopause cold trap for setting the initial condition. The column profile of mole fraction thus obtained is then converted into the corresponding initial specific humidity profile. The resulting saturated region (or that with $\mathrm{RH} = \alpha$ for cases when $\alpha < 100\%$) spans approximately the same vertical range as the CH_4 haze layer in the cloud-and-haze model of Baines and Hammel (1994, their Fig. 1).

We have only one controlling parameter for the initial methane amount, the deep methane molar fraction, and as it happens our results are insensitive to this parameter. The insensitivity is real if the cold-trap idea is valid because for a large range of deep molar fractions, layers 8 and 7 are saturated and hence are fixed, and layers 6 and higher are unsaturated but are likewise fixed, given our bottom-up initialization. The solar C/H number fraction is 0.000398 according to Grevesse and Anders (1991). Assuming $H_2 + He = H_2/0.81$ and $CH_4/H_2 = 2C/H$, then the solar benchmark for Neptune's CH_4 mole fraction is

$$\frac{CH_4}{H_2 + He + CH_4} = \frac{1}{\frac{1}{0.81}\frac{1}{2C/H} + 1} = 0.00064.$$

Baines *et al.* (1995b) determined Neptune's deep tropospheric methane molar fraction to be in the range between 0.016 and 0.027, or 33 ± 9 times the solar value. However, the solar value itself is enough to saturate layers 8 and 7, and so fix layers 8 and upward in the model. Consequently, exactly the same clouds develop in layers 6, 7, and 8 when the deep molar fraction of methane is varied from 1 to 33 times solar. The only change over that range is that in layer 9 ($p \approx 1650$ mb) the maximum RH increases from approximately 1% to 20%, but never enough for clouds to form. It is possible that a different model that recirculates methane upward could exhibit more sensitivity to the deep molar fraction.

2.2. *Transient-Phase Vapor Trimming*

We introduce a Great Dark Spot into the model as a geostrophically balanced anticyclone, an approximation that implies errors on the order of the Rossby number or a few tens of percent. Consequently, when the model is started the vortex undergoes a transient adjustment that lasts about one vortex turn-around time, which is about one week. The resulting wavy disturbances propagate throughout the model and create regions where methane is supersaturated. We have opted to use this initial transient to age the model with respect to its condensable component. During the first 30 days the model is run using a "vapor-trimming" rule similar to that used to set up the initial condition, in which any methane specific humidity in excess of saturation is instantaneously and irreversibly reduced to the amount needed to lower the RH to 100%. The total methane within the model declines over time during this transient phase because the vapor trimming is operated as a sink without any compensating source.

TABLE I
Model Resolution

	This work				LeBeau & Dowling (1998)			
	n	bot	top	Δ	n	bot	top	Δ
lon[a]	128	−60°	60°	0.94°	128	−90°	90°	1.41°
lat[b]	64	−60°	0°	0.94°	64	−90°	0°	1.41°
theta [K][c]	9.5	77	507	varies	10.5	57	652	varies
p [mb][d]	—	1650	5	∼0.5	—	7440	8	0.62
t	—	0 d	40 d	45 s	—	0 d	50 d	50–80 s

[a] Periodic boundary conditions.
[b] Channel boundary conditions.
[c] See Fig. 2.
[d] Initial layer pressures at southern boundary; Δp is in scale heights.

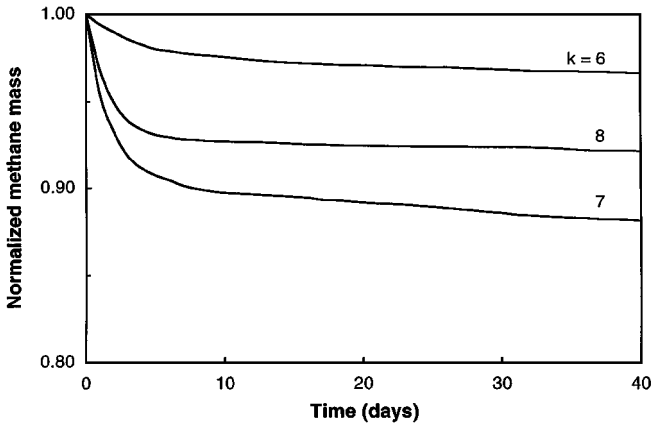

FIG. 3. Loss of methane vs. time for case C due to vapor trimming. The only source of methane in each layer is its initial vapor budget, which equals 0.023, 0.031, 0.051, 0.084, 0.136, 0.303, 1.216, and 70.3×10^{15} kg for layers 2–9, respectively (the horizontal area covered by the model is 1.09×10^9 km^2). In layers 6, 7, and 8 supersaturated regions develop that are dealt with by instantaneously and irreversibly trimming the amount of vapor needed to restore the RH to 100%. There is no exchange of mass between layers because of the $\dot{\theta} = 0$ assumption, and the computed methane budget is constant with time in each layer to $\pm 0.01\%$ or better in the absence of vapor trimming. Because the trimming is unbalanced there is a slow decay of total methane with time; ignoring this, the vapor budget settles into a dynamical equilibrium after an approximately 10-day transient. (In this plot the trimming is always active, but in the rest of the experiments it is turned off at day 30 so that the total vapor in each layer becomes constant.)

The result when vapor trimming is applied continuously for 40 days is shown in Fig. 3 for case C, which is typical. Except for a slow decay due to the unbalanced sink, the transient phase is finished by $t = 10$ days. In all the experiments to follow, the vapor trimming is turned off after 30 days, beyond which the total methane mass is accurately conserved in each layer and any supersaturated regions that develop are left alone and are interpreted to be the sites of nonprecipitating clouds.

2.3. Nonprecipitation Assumption

By assuming no precipitation, we are judging that condensate particles form but that their rainout times are long compared to the relevant dynamical timescales. This is probably not valid for stratus in general on Neptune but should be valid for the orographic clouds considered here based on the following estimate. Assume $g = 11$ m s^{-2}, a dynamic viscosity for hydrogen of $\eta \approx 3 \times 10^{-6}$ Pa s (Weast *et al.* 1987, p. F-45), air density $\rho_a \approx 0.04$ kg m^{-3} (for molar mass $\mu = 2.2$ near Neptune's tropopause), and spherical methane-ice particles with radius a and density $\rho_p \approx 500$ kg m^{-3} (Donnay and Ondik 1972, p. C-9). Particles with Reynolds number Re ≤ 1 (creeping flow) will fall at the Stokes terminal velocity, $U = 2g(\rho_p - \rho_a)a^2/9\eta$, and over a time τ will cover a distance of about $U\tau \approx (35\text{ m})(a/\mu\text{m})^2\,(\tau/\text{day})$. (Since $\text{Re} = 2aU\rho_a/\eta \approx 1 \times 10^{-5}\,(a/\mu\text{m})^3$, the creeping flow assumption is satisfied for particles with radii smaller than about 45 μm.) For a 10,000-km-long cloud with winds moving through at about 45 m s^{-1}, air parcels will only remain in the cloud for about 2 days, during which time a 1-μm radius particle will fall 0.07 km and a 30-μm radius particle will fall 60 km. Assuming the particle radii do not enlarge to tens of micrometers too rapidly, the distance they drop is likely to be small compared to the vertical extent of the bright companion; therefore, retaining the entire methane mass is an acceptable first-order approximation.

2.4. Addition of a GDS

We add a GDS by using essentially the same method described in LeBeau and Dowling (1998). Briefly, one can introduce an eddy that is geostrophically and hydrostatically balanced by specifying the perturbation on the Montgomery streamfunction, $M = H + gz$, where H is the enthalpy, usually written as C_pT for an ideal gas, and gz is the geopotential, both evaluated on θ surfaces. The initial ΔM perturbation used in this study is an ellipsoidal Gaussian of the form

$$\Delta M = u_s \times (1.2\, f_s R_e b_s) \times \exp\left\{-\left[\frac{\phi - \phi_s}{a_s}\right]^2 - \left[\frac{\lambda - \lambda_s}{b_s}\right]^2 - \left[\frac{\ln p - \ln p_s}{c_s}\right]^2\right\}, \qquad (1)$$

where the the subscript "s" stands for "spot." There are seven parameters in (1) that set the initial position and size of the spot: ϕ_s, λ_s, and p_s are the coordinates of the spot's center (ϕ is east longitude, λ is planetographic latitude); a_s, b_s, and c_s set the spot's size (the units of c_s are pressure scale heights); and u_s is the velocity amplitude, which is positive for an anticyclone. The factor $1.2\, f_s R_e b_s$ makes the spot's maximum velocity approximately u_s; it has units of velocity and includes the Coriolis parameter $f_s = 2\Omega \sin\lambda_s$, with the planet's angular velocity $\Omega = 1.083 \times 10^{-4}$ s^{-1}, the equatorial radius $R_e = 24764$ km, and b_s in radians. To skirt computational underflows, ΔM is set to zero when the exponential factor in (1) drops below $\exp(-10) = 4.5 \times 10^{-5}$.

There do not exist direct observations of the vertical position p_s, the vertical extent c_s, or the wind speed u_s in (1) for the GDS-89 or GDS-94. Most of what we know about the vertical extent of giant anticyclones on a gas giant comes from studying Jupiter. Based on the following facts, the standard hypothesis is that Jupiter's vortices are quite thin. First, they merge together in a manner identical to that known to occur in two-dimensional turbulence in rapidly rotating systems (geostrophic turbulence), which is most unlike the behavior of three-dimensional turbulence, where larger eddies break down into smaller ones (e.g., the decay of a smoke ring). A similar test cannot yet be made for Neptune because we have not observed any mutual encounters of vortices on Neptune. Second, on Jupiter the cloud-top absolute vorticity varies by a factor of 2 following the motion around the

largest anticyclones (Dowling and Ingersoll 1988, 1989), which by conservation of potential vorticity means that the effective vertical thickness varies by a factor of 2 also, something a thin object can do much more easily than a thick object. This test also cannot be applied to Neptune's vortices due to lack of eddy wind vectors. Third, the Galileo probe found Jupiter's temperature lapse rate to become nearly adiabatic at depth, the condition expected for a convecting interior and an anticipated result given Jupiter's significant internal heat source and the Voyager radio occultation temperature profile. It is not easy to understand how a large vortex can maintain coherence while penetrating into significant convection. While we do not have an in situ probe of Neptune's atmosphere, both the Voyager radio occultation profile and the existence of a significant internal heat source on Neptune argue for a convecting interior, and hence we tend to favor Great-Red-Spot-analog models of Great Dark Spots that do not penetrate much below the stable outer atmosphere on Neptune.

Since our goal is a qualitative understanding of the bright companion cloud, it may not be necessary to vary all the parameters in (1) or to seek a more realistic initial shape than the ellipsoidal assumption to establish the bright companion clouds as orographic in nature. Accordingly, we keep the following initialization parameters in (1) constant for this study: the horizontal position at $\phi_s = 0^\circ$ and $\lambda_s = -27^\circ$, the horizontal size at $a_s = 20^\circ$ and $b_s = 7^\circ$, and the velocity amplitude at $u_s = 50$ m s^{-1}. As shown in Fig. 2, the vertical size is also kept constant at $c_s = 1.5$ scale heights except for case F, where c_s is reduced to 0.75. The main variable for this work is the initial vertical position of the spot center, p_s, which takes the values $p_s = 50$, 200, 300, 400, and 1000 mbar for cases A, B, C, D, and E/F, respectively. Future work that explores cases where the vertical span is different in the top and bottom halves or extends over more scale heights will add to the diagnostic value of our results.

3. RESULTS

3.1. Temperature Anomaly

A consequence of the thermal-wind relation is that the decay of wind speed with height in the top half of an anticyclone correlates with a negative temperature anomaly (on a given pressure surface the spot is colder in its center than on its periphery), and likewise the decay of wind speed with depth correlates with a positive temperature anomaly. This relation can be used to constrain the vertical structure of a vortex by observing its horizontal temperature field, as has been done for Jupiter's Great Red Spot (Flasar *et al.* 1981). However, the GDS-89 did not show up in Voyager infrared (IRIS) images, except perhaps as a faint depression (Conrath *et al.* 1989), and hence its vertical position is unknown. This is why the initial center position, p_s, is our primary variable. A related point is that to match the data, models of the GDS should not have a large temperature anomaly at the pressure levels observed by IRIS, which extend down to about 1000 mb.

Table II lists the temperature anomaly associated with our model GDS in cases C, D, E, and F at 50 days, on both isentropic and isobaric surfaces. Cases A and B are not listed because the GDS in each of these runs does not survive, as discussed below. The $\Delta T = -1$ K signal generated by the top half of the GDS in cases C and D is significantly less than the $\Delta T = -8$ K dip in temperature associated with Jupiter's Great Red Spot (Flasar *et al.* 1981), but it is on the edge of detectability for Voyager IRIS and hence borders on being too large. The larger positive anomalies in layer 9 would be detectable by Voyager IRIS and were not seen on Neptune; however, if the model's (anomaly-free) abyssal layer, layer 10, is moved deeper this signal will diminish accordingly, which is worth pursuing in a future study. Our view is that cases C–F are stealthy enough with regard to their upper troposphere temperature anomaly to adequately satisfy the IRIS nondetection of the GDS-89 for the purposes of this study.

TABLE II
Model GDS Temperature Anomaly at 50 Days

	ΔT_θ (K)				ΔT_p (K)			
Layer	C	D	E	F	C	D	E	F
5	−1	—	—	—	−1	—	—	—
6	−1	−1	—	—	−1	−1	—	—
7	−1	−1	—	—	−1	−1	—	—
8	6	4	—	—	2	2	—	—
9	2	3	6	5	1	2	3	2

Note. ΔT_θ and ΔT_p give the spot-environment temperature differences along isentropes and isobars, respectively. The model GDS showed no discernible signal on layers 1–4.

3.2. Equatorward Drift

LeBeau and Dowling (1998) isolated the effect of background absolute-vorticity gradient with respect to latitude on the equatorward drift of the GDS by using constant absolute-vorticity-gradient zonal wind profiles, and they found the drift to be proportional to this gradient. Here we do not vary our initial zonal-wind profile from one run to the next, so any variation in drift rate implies that other controlling parameters are acting. Along these lines, an unexpected result is that for the two cases where the top of the GDS is placed in the stratosphere (cases A and B in Fig. 2), the GDS drifts equatorward at a rapid pace and disperses within a matter of weeks. In the first 15 days of case A, the vortex drifts from $\lambda_s = -27^\circ$ latitude to -18°, which is over 10 times faster than the drift of the GDS-89. Three more days pass before it disperses into a wavy perturbation. In case B, the GDS also drifts equatorward in a rapid manner, moving inside of -20° around $t = 25$ days and dispersing by $t = 35$ days.

In contrast, cases C and D drift equatorward at most only a few degrees in 50 days, similar to the GDS-89. The contrast between cases B and C is particularly striking because they differ by only the small shift in initial vertical position of the GDS shown in Fig. 2. Around $t = 45$ days, cases E and F also run into a problem with equatorward drift. Vertical placement is implicated here as

well, but it may be compromised by the fact that the bottom of the GDS in these two cases is close to the bottom of the model.

A search for vertical tilt of the vortex in case A reveals that the potential vorticity (pv) center in layer 6 is offset relative to that in layer 7 by a significant amount, ranging 1.5–3° poleward and 2–5° westward. In case B (dropping down a layer to stay even with the vortex) the pv center in layer 7 is also shifted significantly relative to layer 8, but in the opposite sense than in case A, about 1–2° equatorward and 1–2° eastward. In contrast, case C exhibits no measurable north–south tilt between layers 7 and 8 through 30 days (at 35 days we measure a 1° poleward tilt). The story is different in the east–west direction, because there is a tilt in case C, but it oscillates approximately sinusoidally with an amplitude of about 1° and a period of about 15 days, resulting in no long-term bias. Perhaps a constant bias in vertical tilt is a contributing factor to the rapid equatorward drift of the GDS in cases A and B.

3.3. *Methane Relative Humidity*

We now turn to the interaction of methane vapor with the vortex. Figure 4 illustrates the evolution of potential vorticity and methane RH for case C, displayed with contours and grayscale, respectively. These quantities are illustrated for layers 6, 7, and 8 (top to bottom); none of the other layers had regions with RH $>$ 100% in any of the runs studied. The closed contours of potential vorticity reveal the position, size, and shape of the vortex. The grayscale is chosen so that pure-white regions have RH of 100% or greater. Away from the vortex, the initial RH is 100% in layers 7 and 8 but is subsaturated in layer 6 because the initial condition is set using a tropopause cold trap. Transient wavy disturbances cause the majority of these saturated regions to disappear during the first 10 days of the 30-day vapor-trimming period.

A persistent poleward-rim bright companion can be seen in layer 6 of case C, Fig. 4, top row. As far as we know, this is the first cataloged cloud feature on a gas giant to be reproduced in a GCM. The companion temporarily fades at 40 days; the real companion also occasionally fades as can be seen in the leftmost column of the GDS-89 time sequence in Fig. 4A of Smith *et al.* (1989). An examination of the daily variation in the RH around the vortex reveals that a local maximum is always present on the poleward rim, corresponding to the bright companion, but that the strength of this maximum varies with time. In particular, for the run shown in Fig. 4, the local maximum of RH drops below 100% on day 32, bottoms out around 85% 2 days later and stays there for the next 2 days (34–36), and then hovers around 95% until day 44 when it again moves above 100%. The RH stays above 100% for another 11 days and then dips down and hovers around 92% from day 55 to the end of the run at day 60. Interestingly, when the companion disappears the first time, days 32–43, the supersaturated region rotates in

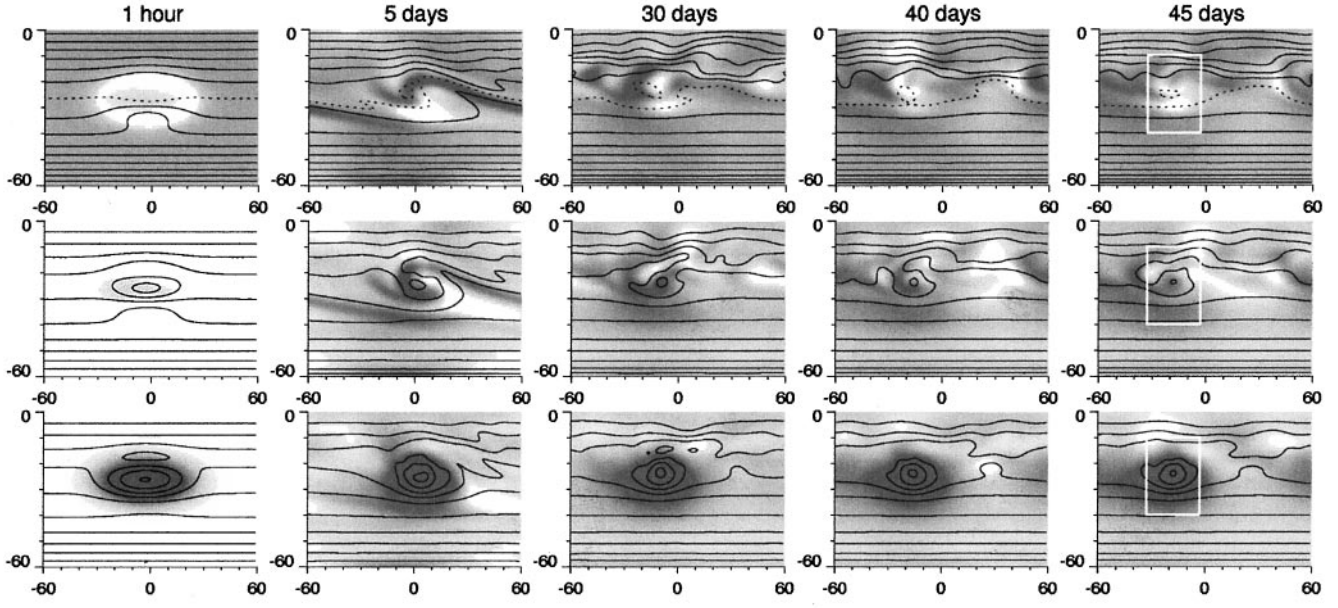

FIG. 4. Time evolution of methane relative humidity for case C. In each panel the ordinate is latitude and the abscissa is longitude in degrees, with channel boundary conditions at latitudes $-60°$ and $0°$ and periodic boundary conditions at longitudes $\pm 60°$. The top, middle, and bottom of each column corresponds to levels 6, 7, and 8, respectively. In all the runs examined these are the only layers that contain sites where RH $\geq$ 100%, which are shown here as white to indicate cloud locations. After a transient phase that lasts about 10 days, the range of RH settles to be approximately 70–100% in layers 6 and 7 and approximately 30–100% in layer 8. Circulation patterns are revealed by contours of potential vorticity at intervals of 1.1, 0.53, and 0.21 PVU for layers 6, 7, and 8, respectively (1 PVU $= 10^{-6}$ m^2 s^{-1} K kg^{-1}). Across the top row (layer 6), an open contour (-6.8 PVU) that threads a poleward bright companion is distinguished by a dotted line; we dub this the "ride" contour. A segment of this contour pinches off during the run. The variation of thermodynamical quantities along the ride contour is shown in Fig. 5, and the zoom box in the last column corresponds to the upper-left panel of Fig. 6.

the anticyclonic direction (counterclockwise) from a southern position to an eastern position and then moves in toward the spot's center. A new supersaturated region then appears at the normal companion position. The disappearance at day 55 is somewhat different, with more than one cloud showing up near the typical southern-rim position but none exactly on it.

The time spent below RH = 100% by our model bright companion is somewhat longer than the fading episodes of the actual GDS-89. However, the two may be quite similar when one considers that clouds can be visible when the bulk RH, which is what we are reporting, is less than 100%. Additional progress here will require cloudiness parameterizations of the type developed by Xu and Randall (1996).

The line of potential vorticity that threads through the companion in Fig. 4 is an open contour, one that encircles the planet, and provides a first-order indication of the path followed by moving air parcels (it is approximate because the system is not steady). In this simulation the GDS drifts in longitude at the steady rate of -72.6°/day, which corresponds to -314 m s^{-1} at the bright companion latitude of -30.3°. Moist air approaches the GDS from the west, moves through the bright companion at $u = -269$ m s^{-1}, which is 45 m s^{-1} eastward in the GDS reference frame, and then continues eastward away from the GDS. For future reference, we dub this the "ride" contour and highlight it with a dotted line in Fig. 4.

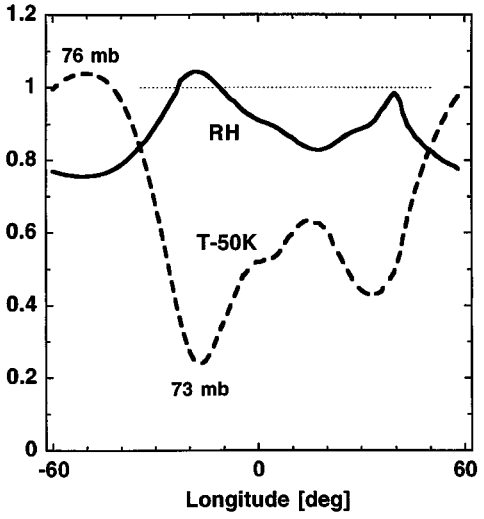

FIG. 5. Variation of thermodynamical variables following the motion through a bright companion. The solid curve is methane RH along the ride streamline in layer 6 at $t = 45$ days (the dotted open contour in the upper-right panel of Fig. 4). The dashed curve is the temperature (minus 50 K) along the streamline; it varies by less than 1 K. The pressure varies by about 3 mb and has its minimum in the cloud region. This streamline rises about half a kilometer to clear the top of the anticyclone.

An intermittent long cloud to the east of the model GDS in layer 7 tends to mimic the real eastern long cloud. After 40 days there is some residual cloudiness scattered about that is unrelated to the GDS, especially near 10°S in layer 8, and which does not correspond to clouds seen on Neptune. This overabundance of clouds in the model could be remedied by adjusting the initialization scheme to reduce the amount of methane vapor in layer 8. However, since this problem is not central to the testing of the orographic-cloud hypothesis, we leave it alone for now.

Figure 5 shows the Lagrangian viewpoint of the formation of a bright companion along the ride contour in the upper-right panel of Fig. 4. The quantities of interest are interpolated from the model grid onto this path. The figure shows the methane RH as the solid line and temperature (minus 50 K) as the dashed line; there is less than 1 K variation in temperature along the entire ride. Pressure is not plotted because it closely resembles temperature, but instead it is labeled at its maximum outside the cloud, $p = 76$ mb, and at its minimum inside the cloud, $p = 73$ mb. The pressure scale height is $RT/g \approx (3480)(50)/(11) \approx 16$ km, so this 4% drop in pressure corresponds to a lift of about half a kilometer. These results, in combination with the 45 m s^{-1} winds blowing through the cloud and its smooth, elongated appearance, suggest that it is an orographic cloud.

The simulations show a tendency for clouds to be more stable along the poleward rim than the equatorward rim of the GDS, which is consistent with the position of the real bright companions, Fig. 1. One cause of this asymmetry appears to be that the winds on the poleward side blow straighter and steadier than their equatorward counterparts; therefore, the moist air is not lifted until it gets right on top of the vortex, and this occurs in a consistent manner. In contrast, the equatorward winds are more turbulent, with a tendency to trip the cloud early. It is probably not the case that there is more methane streaming into the poleward side of a GDS than the equatorward side, which would yield a preference for poleward clouds. The shape oscillation (Kida oscillation) of a GDS produces a chaotic zone that is likely to keep the methane vapor fairly well mixed, in the same manner that Polvani *et al.* (1990) found it homogenizes the potential vorticity in a latitudinal band around the GDS. In our model, the methane vapor starts out evenly distributed and tends to remain so.

The intermittent clouds that form on the equatorward side of the model GDS are often caught up in the vortex itself, as in the top row in Fig. 4, or are buffeted by small, break-away eddies of potential vorticity, whereas the poleward cloud is threaded by open streamlines that are steady and smooth. In the bottom row in Fig. 4 (layer 8) one can see that the potential vorticity gradient is weaker on the equatorward side of the vortex, and in the middle row (layer 7) it can reverse sign, which suggests that shear instability may play a role in disrupting the winds and clouds on the equatorward side.

Figure 6 shows the three-dimensional location of the clouds relative to the vortex. Depicted are top and side views of the RH = 100% isosurface (white) for cases C, D, E, and F. The GDS is indicated by the $\zeta' = 0.08 \times 10^{-4}$ s^{-1} eddy relative vorticity isosurface (blue). Eddy relative vorticity is defined as the vertical component of the curl of the velocity minus the zonal average. It is used here instead of potential vorticity because it is not divided by density and therefore can be directly compared

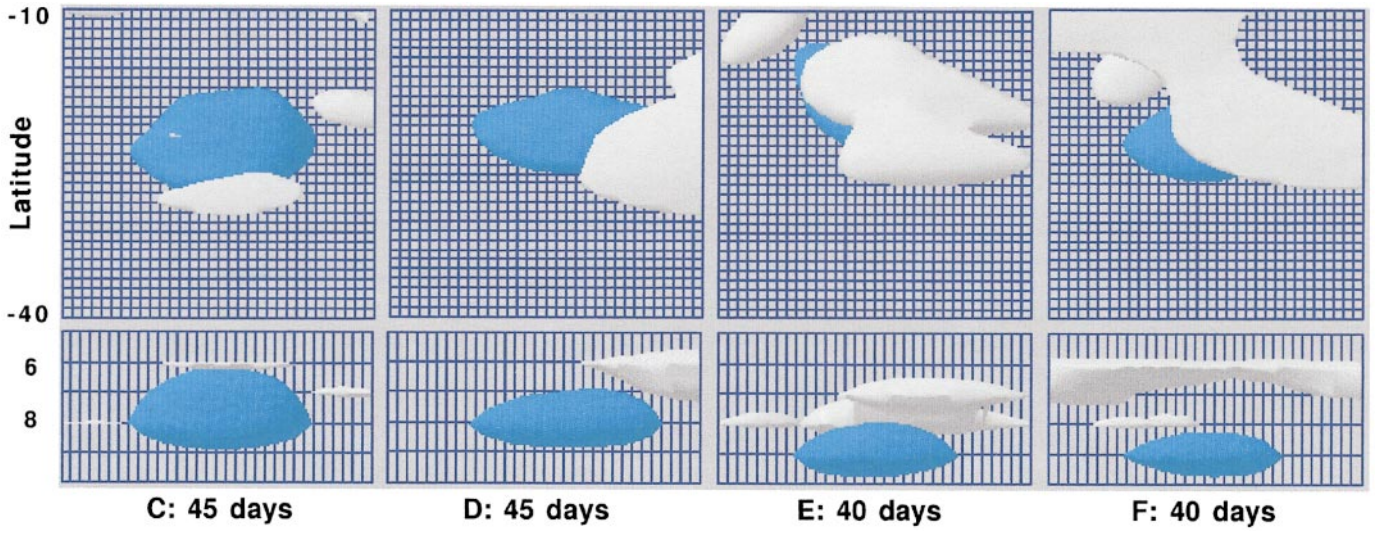

FIG. 6. Isosurfaces of 100% RH (white) and 0.08×10^{-4} s^{-1} eddy relative vorticity (blue). Cases C and D are shown at $t = 45$ days; cases E and F are shown 5 days earlier because the GDS begins to drift equatorward and disperse around 45 days; cases A and B are not shown because the GDS disperses before 40 days. The upper image in each column is the view from above and covers the latitude range -40° to -10° and the longitude range $\pm 15^\circ$ centered on the GDS; the gridlines are indicated at 0.94° intervals. The upper-left panel corresponds to the zoom box in Fig. 4. The lower image in each pair is the side view looking north; the horizontal gridlines mark the isentropic layer centers rather than the layer interfaces, with the tropopause at $k = 6$. Refer to Fig. 2 to relate the model's isentropic layers to pressure. Fluid motion is strictly horizontal in this plot because of the assumption that $\dot{\theta} = 0$. The vertical dimension in the lower panels is exaggerated by a factor of about 150 in terms of true shape. Lighting from a single point source (with no cast shadows) helps to visualize the shape of the isosurfaces and has no other significance.

between layers. For reference, at -27°S the Coriolis parameter is $f = -0.99 \times 10^{-4}$ s^{-1} and the zonal average of relative vorticity is $\bar{\zeta} \approx 0.30 \times 10^{-4}$ s^{-1}. The zoom box in the last column of Fig. 4 corresponds to the upper-left panel in Fig. 6 and is useful for orientation and for comparing the size of this particular ζ' isosurface to the size of closed potential-vorticity contours. We note a trend toward increased cloudiness as the GDS altitude is dropped from case C to D to E/F, the most realistic simulation being case C. This, combined with the fate of the GDS in cases A and B, suggests that the top of the GDS (defined in the sense of (1)) is at the tropopause. The position of its bottom is not well constrained, except that it might need to be moved slightly deeper than the models considered here to reduce its positive temperature anomaly (Table II).

We are interested in how low the initial RH in layers 6, 7, and 8 can be reduced and still produce a RH $\geq 100\%$ bright companion. For case C, we tried reduction factors α equal to 1.00, 0.93, 0.80, and 0.70. After the vapor trimming period, the corresponding average values of RH in layer 6 became 86%, 81%, 72%, and 63%. In the latter two cases the RH of the bright companion dropped below 100%, so we conclude that an average RH of about 80% or more near the tropopause is needed to produce a substantial bright companion.

3.4. *Cloud Properties*

The optical depth of clouds associated with the model's supersaturated regions may be estimated by assuming all the excess methane vapor condenses into spherical cloud particles of radius a, density ρ_p, and mass $m_p = \rho_p 4\pi a^3/3$. Define the excess specific humidity of methane (the amount above saturation) to be $\Delta q_{CH_4} = \Delta\rho_{CH_4}/\rho$, where ρ is the total density and $\Delta\rho_{CH_4}$ is the difference in methane vapor density between our actual specific humidity and the saturated value. For a layer of geometrical thickness Δz, the mass per unit area to be condensed into cloud particles is $\Delta\sigma_{CH_4} = \Delta z\, \rho\, \Delta q_{CH_4} = (|\Delta p|/g)\Delta q_{CH_4}$, assuming hydrostatic balance, where Δp is the pressure-thickness of the layer and g is gravity. The number of cloud particles per unit area is then

$$n_p = \frac{\Delta\sigma_{CH_4}}{m_p} = \frac{3}{4\pi}\frac{1}{\rho_p}\frac{|\Delta p|}{g}\frac{\Delta q_{CH_4}}{a^3}. \tag{2}$$

For wavelengths smaller than $2\pi a$ the extinction cross section is approximately twice the geometrical area, and hence the optical depth is approximately

$$\tau \approx 2\pi a^2 n_p = \frac{3}{2}\frac{1}{\rho_p}\frac{|\Delta p|}{g}\frac{\Delta q_{CH_4}}{a}. \tag{3}$$

The maximum RH in Fig. 5 occurs at longitude -18° and has the value 1.043 (i.e., 104.3%). The specific humidity of methane at this point is $q_{CH_4} = 3.54 \times 10^{-4}$ and the excess above saturation is $\Delta q_{CH_4} = 1.52 \times 10^{-5}$. Layer 6 covers $|\Delta p| \approx |90\text{–}60|$ mb $= 3000$ Pa, which with $\rho_p = 500$ kg m^{-3} implies the bright companion in case C has an optical depth of $\tau \approx 1.2$ ($10\ \mu$m$/a$), where a is the cloud-particle radius.

Some observational information exists on the radius of Neptune's methane cloud particles. Figure 7 of Conrath *et al.* (1991) shows a weak dependence in synthetic spectra of methane cloud

models in the 220 to 325 cm^{-1} wavenumber range where the atmosphere is tranparent enough to allow emission from the underlying clouds to contribute to the outgoing radiation field. They applied the method to Voyager IRIS spectra covering latitudes near 39–45°S and found that radii fall between 0.3 and 30.0 μm. Figure 6 of Baines and Hammel (1994) shows a plausible range of methane haze particle radii to be 0.2–4.0 μm, based on their center-to-limb analysis of three methane bands. It is not known whether either of these sampled cloudiness conditions are representative of those inside an orographic bright companion, but if they are then the relation for the optical depth above implies that the clouds we are predicting are observable.

Our neglect of latent heating can be justified a posteriori. The temperature increase from condensation is

$$\Delta T = x\frac{L_{CH_4}}{c_p}, \tag{4}$$

where L_{CH_4} is the molar enthalpy of sublimation of methane, x is the methane mole fraction that undergoes condensation, and c_p is the molar specific heat of air. Appropriate values are $L_{CH_4} = 1 \times 10^4$ J mol^{-1} (Atreya 1986, p. 57) and $c_p = 21$ J $mol^{-1}K^{-1}$ (which is $2.5R$, appropriate for helium and for cold hydrogen for processes that are too fast for ortho–para hydrogen conversion; see Farkas (1935)). The value $\Delta q_{CH_4} = 1.52 \times 10^{-5}$ above implies $x = (\mu/\mu_{CH_4})\Delta q_{CH_4} = 2.1 \times 10^{-6}$, such that $\Delta T = 0.001$ K. The heating is small because the clouds occur around 100–300 mbar where the methane saturation vapor pressure is low. Similar RH values in layers 7 and 8 would imply heating close to 0.001 and 0.01 K, respectively. Only if methane condensation were to occur around 1 bar would latent heating reach a few degrees and become significant.

4. DISCUSSION

We have demonstrated by construction the feasibility of the orographic-cloud hypothesis for the formation of companion clouds to Neptune's Great Dark Spots. Open streamlines near the tropopause that pass over the GDS anticyclone experience a small drop in pressure and temperature that is sufficient to raise the methane relative humidity from around 80% to over 100%, resulting in observable methane clouds. Companion clouds can also form about a hundred millibars below the tropopause. No clouds formed above the tropopause.

We have evidence from our simulations that the top of the GDS is at the tropopause. If we initialize an anticyclone with its top above the tropopause, it drifts toward the equator at a rate that is an order of magnitude faster than has been observed. This is interesting behavior and deserves further study. When the top of the vortex is positioned below the tropopause the model produces companion clouds that are larger than observed for the GDS-89, whereas they resemble the observations when the top is at the tropopause.

Part of the answer of why the poleward rim of the GDS favors formation of coherent clouds relative to the equatorward side is that the winds on the poleward side are smooth, whereas the winds on the equatorward side are turbulent. In our model, it is not so much that there are fewer clouds on the equatorward side but that they are less steady and less stationary. The root cause for this asymmetry may be a shear instability on the equatorward side of the vortex, as suggested by the existence of weakened and reversed potential vorticity gradients.

At least two important observational details about bright companions have been missed by these simulations but should be attainable in the near future. The first is the tendency for white clouds on Neptune (and Uranus) to consist of a multitude of thin parallel clouds. The images in Fig. 1 do not have high enough resolution to show this, but it can be seen in Figs. 3 and 4 of Smith *et al.* (1989). It is probable that there is useful diagnostic information in the spacing of these narrow cloud bands; for example, they may be modulated by the phase of gravity waves. An increase in meridional and vertical resolution in a model such as ours may be what is needed to address this question.

The second missed detail is the bright complex of clouds extending from the GDS-94 toward and past the equator in the second image from the bottom-left of Fig. 1 and the similar but smaller white cloud just past the equator from the GDS-89 in the rightmost bottom image (which is flipped across the equator). These long-distance companions pace their respective great spots for substantial periods of time and are quite remarkable, perhaps unique to Neptune. An idea put forward by Sromovsky *et al.* (2001) is that this may be an equatorial Kelvin wave attached to the GDS. We suspect that this phenomenon is unique to Neptune because Uranus and Saturn do not have great spots and Jupiter's equatorial winds blow in the wrong direction, at least for the Kelvin-wave idea.

It would be interesting to focus next on the formation of white clouds on Neptune and Uranus that are not tripped into existence by a vortex. In particular, why is it common for bright clouds to populate certain latitude bands and not others? In this problem the effects of latent heating and precipitation are likely to play a role, and the payoff will be an increased understanding of the diabatic circulation.

ACKNOWLEDGMENTS

We thank Andrew Ingersoll and an anonymous referee for their helpful comments. This research was supported by the NASA Planetary Atmospheres Program (Grant NAGS-6913), the Space Telescope Science Institute (Grants AR-06374.01, GO-06650.01-95A, and GO-07324.03-96A), and the National Research Council. It uses observations with the NASA–ESA Hubble Space Telescope, obtained at the Space Telescope Science Institute, which is operated by the Association of Universities for Research in Astronomy, Inc., under NASA Contract NAS5-26555.

REFERENCES

Atreya, S. K. 1986. *Atmospheres and Ionospheres of the Outer Planets and Their Satellites.* Springer-Verlag, New York.

Baines, K. H., and H. B. Hammel 1994. Clouds, hazes, and the stratospheric methane abundance in Neptune. *Icarus* **109**, 20–39.

Baines, K. H., H. B. Hammel, K. A. Rages, R. N. Romani, and R. E. Samuelson 1995a. Clouds and hazes in the atmosphere of Neptune. In *Neptune and Triton*, (D. P. Cruikshank, Ed.), pp. 489–546. Univ. of Arizona Press, Tucson.

Baines, K. H., M. E. Mickelson, L. E. Larson, and D. W. Ferguson 1995b. The abundances of methane and ortho/para hydrogen in Uranus and Neptune: Implications of new laboratory 4-0 H-2 quadrupole line parameters. *Icarus* **114**, 328–340.

Carlson, B. E., W. B. Rossow, and G. S. Orton 1988. Cloud microphysics of the giant planets. *J. Atmos. Sci.* **45**, 2066–2081.

Conrath, B. J., F. M. Flasar, R. Hanel, V. Kunde, W. Maguire, J. Pearl, J. Pirraglia, R. Samuelson, P. Gierasch, A. Weir, B. Bezard, D. Gautier, D. Cruikshank, L. Horn, R. Springer, and W. Shaffer 1989. Infrared observations of the neptunian system. *Science* **246**, 1454–1459.

Conrath, B. J., B. Gautier, G. F. Lindal, R. E. Samuelson, and W. A. Shaffer 1991. The helium abundance of Neptune from Voyager measurements *J. Geophys. Res.* **96**, 18907–18919.

Donnay, J. D. H., and H. M. Ondik 1972. *Crystal Data Determinative Tables Vol. I: Organic Compounds*, 3rd ed., Natl. Bur. of Standards, Washington, DC.

Dowling, T. E., and A. P. Ingersoll 1988. Potential vorticity and layer thickness variations in the flow around Jupiter's Great Red Spot and White Oval BC. *J. Atmos. Sci.* **45**, 1380–1396.

Dowling, T. E., and A. P. Ingersoll 1989. Jupiter's Great Red Spot as a shallow water system. *J. Atmos. Sci.* **46**, 3256–3278.

Dowling, T. E., A. S. Fischer, P. J. Gierasch, J. Harrington, R. P. LeBeau, and C. M. Santori 1998. The explicit planetary isentropic-coordinate (EPIC) atmospheric model. *Icarus* **132**, 221–238.

Farkas, A. 1935. *Orthohydrogen, Parahydrogen, and Heavy Hydrogen*. Cambridge University Press, Cambridge.

Flasar, F. M., B. J. Conrath, J. A. Pirraglia, P. C. Clark, R. G. French, and P. J. Gierasch 1981. Thermal structure and dynamics of the jovian atmosphere 1. The Great Red Spot. *J. Geophys. Res.* **86**, 8759–8767.

Grevesse, N., and E. Anders 1991. Appendix A: Solar Element Abundances, Table 1. In *Solar Interior and Atmosphere* (A. N. Cox, W. C. Livingston, and M. S. Matthews, Eds.), pp. 1229–1230. Univ. of Arizona Press, Tucson.

Hammel, H. B., G. W. Lockwood, J. R. Mills, and C. D. Barnet 1995. Hubble space telescope imaging of Neptune's cloud structure in 1994. *Science* **268**, 1740–1742.

Houze, R. A. 1994. *Cloud Dynamics*. Academic Press, San Diego.

Hsu, Y. J. G., and A. Arakawa 1990. Numerical modeling of the atmosphere with an isentropic vertical coordinate. *Mon. Weather Rev.* **118**, 1933–1959.

Johnson, D. R., T. H. Zapotocny, F. M. Reames, B. J. Wolf, and R. B. Pierce 1993. A comparison of simulated precipitation by hybrid isentropic-sigma and sigma models. *Mon. Weather Rev.* **121**, 2088–2114.

LeBeau, R. P., and T. E. Dowling 1998. EPIC simulations of time-dependent, three dimensional vortices with application to Neptune's Great Dark Spot. *Icarus* **132**, 239–265.

Polvani, L. M., J. Wisdom, E. DeJong, and A. P. Ingersoll 1990. Simple dynamical models of Neptune's Great Dark Spot. *Science* **249**, 1393–1398.

Romani, P. N., J. Bishop, B. Bézard, and S. Atreya 1993. Methane photochemistry on Neptune: Ethane and acetylene mixing ratios and haze production. *Icarus* **106**, 442–463.

Showman, A. P., and T. E. Dowling 2000. Nonlinear simulations of Jupiter's 5-micron hot spots. *Science* **289**, 1737–1740.

Smith, B. A., L. A. Soderblom, B. Banfield, C. Barnet, A. T. Basilevsky, R. F. Beebe, K. Bollinger, J. M. Boyce, A. Brahic, G. A. Briggs, R. H. Brown, C. Chyba, S. A. Collins, T. Colvin, A. F. Cook, D. Crisp, S. K. Croft, D. Cruikshank, J. N. Cuzzi, G. E. Danielson, M. E. Davies, E. De Jong, L. Dones, D. Godfrey, J. Goguen, I. Grenier, V. R. Haemmerle, H. Hammel, C. J. Hansen, C. P. Helfenstien, C. Howell, G. E. Hunt, A. P. Ingersoll, T. V. Johnson, J. Kargel, R. Kirk, D. I. Kuehn, S. Limaye, H. Masursky, A. McEwen, D. Morrison, T. Owen, W. Owen, J. B. Pollack, C. C. Porco, K. Rages, P. Rogers, D. Rudy, C. Sagan, J. Schwartz, E. M. Shoemaker, M. Showalter, B. Sicardy, D. Simonelli, J. Spencer, L. A. Sromovsky, C. Stoker, R. G. Strom, V. E. Suomi, S. P. Synott, R. J. Terrile, P. Thomas, W. R. Thompson, A. Verbiscer, and J. Veverka 1989. Voyager 2 at Neptune: Imaging science results. *Science* **246**, 1422–1449.

Sromovsky, L. A., P. M. Fry, T. E. Dowling, K. H. Baines, and S. S. Limaye 2001. Coordinated 1996 HST and IRTF observations of Neptune and Triton. III. Neptune's atmospheric circulation and cloud structure. *Icarus* **146**, 459–488.

Sromovsky, L. A., S. S. Limaye, and P. M. Fry 1993. Dynamics of Neptune's major cloud features. *Icarus* **105**, 110–141.

Stoker, C. R., and O. B. Toon 1989. Moist convection on Neptune. *Geophys. Res. Lett.* **16**, 929–932.

Thompson, W. T., T. Haack, J. D. Doyle, and S. D. Burk 1997. A nonhydrostatic mesoscale simulation of the 10–11 June 1994 coastally trapped wind reversal. *Mon. Weather Rev.* **125**, 3211–3230.

Tiedtke, M. 1993. Representation of clouds in large-scale models, *Mon. Weather Rev.* **121**, 3040–3061.

Weast, R. C., M. J. Astle, and W. H. Beyer, Eds. 1987. *CRC Handbook of Chemistry and Physics*, 68th edition. CRC Press, Boca Raton, Florida.

Xu, K.-M., and D. A. Randall 1996. A semiempirical cloudiness parameterization for use in climate models. *J. Atmos. Sci.* **53**, 3084–3102.